Crossover From Nanoscopic Intergranular Hopping to Conventional Charge Transport in Pyrite Thin Films

Xin Zhang, Michael Manno, Andrew Baruth, Melissa Johnson, Eray S. Aydil, and Chris Leighton*

Department of Chemical Engineering and Materials Science, University of Minnesota, Minneapolis, Minnesota 55455, United States

ABSTRACT Pyrite FeS_2 is receiving a resurgence of interest as a uniquely attractive thin film solar absorber based on abundant, low-cost, nontoxic elements. Here we address, *via ex situ* sulfidation synthesis, the long-standing problem of understanding conduction and doping in FeS_2 films, an elusive prerequisite to successful solar cells. We find that an abrupt improvement in crystallinity at intermediate sulfidation temperatures is accompanied by unanticipated crossovers from intergranular hopping to conventional transport, and, remarkably, from hole-like to electron-like Hall coefficients. The hopping is found to occur between a small volume fraction of conductive nanoscopic sulfur-deficient grain cores (beneath our X-ray diffraction detection limits), embedded in nominally stoichiometric FeS_2. In addition to placing constraints on the conditions under which useful properties can be obtained from FeS_2 synthesized in diffusion-limited situations, these results also emphasize that FeS_2 films are *not* universally p-type. Indeed, with no knowledge of the active transport mechanism we demonstrate that the Hall coefficient alone is insufficient to determine the sign of the carriers. These results elucidate the possible transport mechanisms in thin film FeS_2 in addition to their influence on the deduced carrier type, an enabling advancement with respect to understanding and controlling doping in pyrite films.

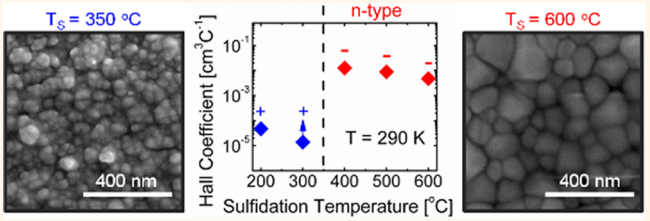

KEYWORDS: iron pyrite · photovoltaics · hopping conduction · Hall effect · doping

The development of photovoltaic (PV) materials suitable for large-scale deployment of solar-to-electric power conversion devices is one of the biggest challenges of our time. Ideal materials would not only display high absorption in the visible, enabling use of thin film solar cells to minimize materials costs, but would also comprise earth-abundant, low-cost, nontoxic elements, amenable to large-scale production.[1,2] While the materials dominating the current PV market (Si, CdTe, and $CuInGaSe_2$) each offer unique advantages, none are able to satisfy *all* of these requirements.[1,2] For example, the indirect band gap of crystalline Si leads to relatively poor solar absorption and thus to the need for high thickness (and materials costs), while CdTe and $CuInGaSe_2$ suffer from concerns over either low earth abundance of some of their constituents (*e.g.*, In, Te), toxicity (*e.g.*, Cd), or both.[1,2]

Pyrite structure FeS_2 on the other hand, has long been acknowledged as a material with outstanding potential to satisfy these criteria.[1,2] The pyrite band gap lies in a useful region (~0.95 eV) and the absorption coefficient exceeds a remarkable 10^5 cm^{-1} above 1 eV, rendering a thickness of <100 nm sufficient to absorb >90% of sunlight.[2] This can be compared to >200 μm for Si.[3] It is thus unsurprising that, from the mid 1980s, significant research focused on the development of FeS_2-based PV.[2] Having yielded cell efficiencies <3% and open circuit voltages of only ~0.1 V, this effort was not entirely successful.[2−4] Although no single origin for these disappointing results emerged, a number of serious issues were identified.[2−4] Prominent among these is that thin film FeS_2 conduction and doping mechanisms are poorly understood. In particular, crystals are typically n-type,[2−5] while, in the majority of cases, thin films appear to exhibit p-type conduction.[2−4] This is not understood, and indeed the primary electrically active defects expected in FeS_2 remain a matter of debate.[3,6−8] One important consequence of this inability to understand doping in FeS_2 films is that the work evolved away from

* Address correspondence to leighton@umn.edu.

Received for review January 21, 2013 and accepted February 24, 2013.

Published online February 25, 2013
10.1021/nn4003264

potentially simpler p−n homojunction or p−i−n cells, instead favoring photoelectrochemical and metal/FeS_2 Schottky-type devices.[2] The failure of such devices to yield large open circuit voltages or efficiencies has been interpreted many ways, the existence of uncontrolled surface states and defects being one widely cited example.[2−4] Given these difficulties, and the emergence of materials such as CdTe and $CuInGaSe_2$, interest in FeS_2 films for PV waned.

Very recently, the outstanding potential of FeS_2 as a solar absorber, in tandem with the minimal toxicity and low costs of Fe and S, has stimulated renewed interest. New synthesis routes are being explored,[3,4,9−12] substantial efforts are being made to understand defects/doping[3,4,7,8] and surfaces/interfaces,[4,9,13] and properties are being revisited.[3,4,9] It is in this context that we have performed a detailed study of electronic conduction in thoroughly characterized FeS_2 thin films synthesized *via* one of the simplest techniques: *ex situ* sulfidation of Fe.[14−20] The results reveal a significant surprise. Specifically, as the sulfidation temperatures are increased above 400−450 °C we observe a crossover in the conduction mechanism, from hopping to a more conventional band transport-type mechanism. Through detailed analysis of the transport parameters, characterization of the Fe spin-state, and simple calculations on S diffusion, we demonstrate that this hopping occurs *via* conductive S-deficient nanoscopic grain cores (at volume fractions beneath typical lab X-ray detection limits), embedded in nominally stoichiometric FeS_2. As the sulfidation temperature is increased, and diffusion improves, this gives way to more conventional transport. The implications in terms of expectations for device performance from films synthesized under diffusion-limited conditions are quite clear. Moreover, the conduction crossover is found to be accompanied by an abrupt sign reversal of the Hall coefficient, from hole-like (in the hopping regime) to electron-like. In addition to emphasizing the need to fully understand transport mechanisms in order to reliably interpret the sign of the Hall coefficient, our findings also highlight that FeS_2 thin films are *not* universally p-type.

RESULTS AND DISCUSSION

As described in more detail in the Methods section and in Supporting Information (SI), FeS_2 films were prepared by *ex situ* sulfidation of 33 nm thick Fe films on Al_2O_3(0001) at sulfidation temperatures, T_S, between 100 and 800 °C. Wide-angle X-ray diffraction (WAXRD) data as a function of T_S are shown in Figure 1. As discussed in SI, these data were obtained by integrating 2D area scans, and are normalized to thickness, and intensity of the Al_2O_3 (0006) substrate peak. Expected powder patterns for pyrite FeS_2, marcasite FeS_2 (the well-known FeS_2 polymorph), and metallic Fe are shown for comparison. Below 200 °C, although

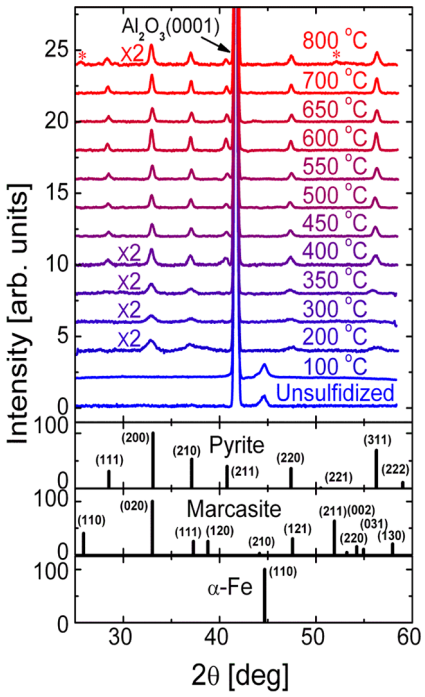

Figure 1. X-ray Diffraction Characterization. Wide-angle X-ray diffraction from Al_2O_3(0001)/Fe films (original thickness 33 nm) sulfidized at temperatures between 100 and 800 °C. An unsulfidized film is shown for comparison. The bottom panels show comparisons to pyrite FeS_2, marcasite FeS_2, and Fe powder patterns. Marcasite peaks in the experimental data (at 800 °C) are labeled with an asterisk.

energy dispersive spectroscopy (EDS) detects ∼5 atom % S, only the reflections from metallic Fe are observed, indicating that crystalline Fe−S compounds do not yet form in detectable quantities. This changes radically at $T_S \geq 200$ °C (in reasonable agreement with prior work),[15,18] where multiple peaks indexable to pyrite FeS_2 are observed, growing in intensity with T_S, particularly above 400 °C. Only at $T_S = 800$ °C is any evidence for a minor marcasite impurity phase found (peaks labeled with an asterisk). We thus conclude, with the usual caveats regarding WAXRD detection limits, that single-phase,[21] nominally untextured, pyrite FeS_2 is obtained over a wide range of T_S from 200 to 700 °C. Scanning electron microscopy (SEM) images of films sulfidized between 200 and 700 °C are shown in Figure 2, in both plan (top panel) and tilt (bottom panel) views. At $T_S \leq 400$ °C we find a dense array of quite monodisperse ∼60 nm diameter grains, forming relatively smooth polycrystalline films.[22] Above 400 °C however, rapid grain growth occurs, accompanied by an increase in surface roughness and faceting as the grain size approaches the thickness. Somewhat similar behavior has been observed in prior work on *ex situ* sulfidation.[15,16,18,19] At T_S values such as 600 °C (Figure 2d,i) we obtain films that are essentially a monolayer of ∼100 nm diameter FeS_2 grains, a desirable microstructure for PV applications. At even higher T_S (*e.g.*, 700 °C, Figures 2e,j) discontinuity and delamination

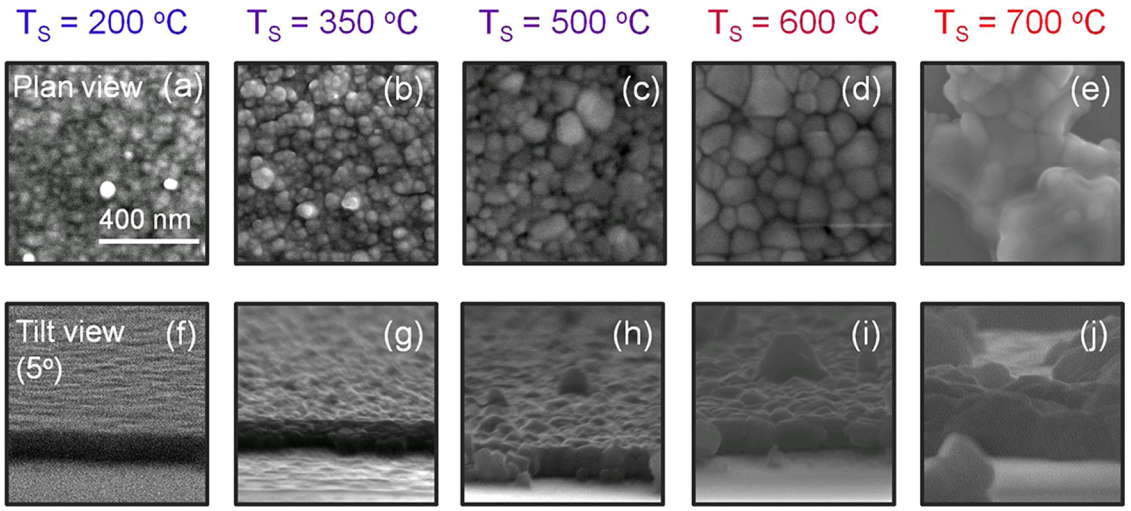

Figure 2. Scanning electron microscopy. Plan-view (a–e) and tilt-view (5° from the substrate plane, (f–j)) secondary electron SEM images (15 kV accelerating voltage) of Al_2O_3(0001)/Fe films (original thickness 33 nm) sulfidized at representative temperatures of 200, 350, 500, 600, and 700 °C.

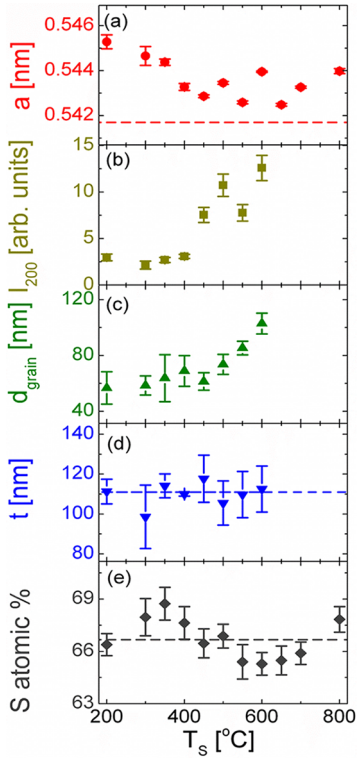

Figure 3. Structural and chemical characterization summary. Sulfidation temperature (T_S) dependence of (a) the lattice parameter (a), (b) the integrated and normalized intensity of the (200) pyrite FeS_2 wide-angle X-ray diffraction peak (I_{200}), (c) the in-plane grain size from SEM (d_{grain}), (d) the final film thickness from tilt-view SEM images (t) (the original Fe thickness was 33 nm), and (e) the S atomic % from EDS. The horizontal dashed lines in panels a, d, and e correspond to the bulk lattice parameter, final thickness based on expected expansion ratio, and ideal stoichiometry, respectively.

occur.[23] This is in the temperature range at which pyrite decomposition is likely to become an issue under these conditions. The transport studies that are the major focus of this paper thus focus on 200 °C ≤ T_S ≤ 600 °C.

Quantification of the results from Figure 1 and 2, and additional characterization data, are shown as a function of T_S in Figure 3, which plots (a) the lattice parameter (a) from WAXRD, (b) the normalized intensity of the (200) pyrite WAXRD peak (I_{200}), (c) the lateral grain size (d_{grain}) from SEM, (d) the film thickness (t) from tilted SEM, and (e) the S content from EDS. The out-of-plane lattice parameter (Figure 3a) is expanded by ~0.5% with respect to bulk (horizontal dashed line). Variations in lattice parameter have been reported for multiple FeS_2 deposition methods [*e.g.*, refs 16, and 24], and could be related to point defects,[16] or, potentially, strain. We note, (i) that the expansion observed here is comparable in magnitude to other work[24] and (ii) that our data provide evidence of an approach to the bulk value above 400 °C, perhaps implying lower defect density or the onset of strain relaxation. Panels b and c illustrate more quantitatively the trends in Figures 1 and 2, a substantial increase in I_{200} and d_{grain} occurring above T_S ≈ 400–450 °C. As can be seen from Figure 3d, the final film thicknesses are essentially independent of T_S above 200 °C, the expansion factor (~3.4) lying close to theoretical estimates for Fe to FeS_2 conversion, again consistent with nominally phase-pure FeS_2. Finally, from Figure 3e it is seen that the S content is only weakly T_S-dependent. Some evidence for S excess is found at 200 C < T_S < 400 °C, perhaps consistent with the expanded lattice parameter (Figure 3a). Additional characterization for 200 °C ≤ T_S ≤ 600 °C is provided in the Supporting Information, demonstrating a uniform Fe:S ratio through the film depth (from Auger electron spectroscopy (AES)), in addition to further evidence of phase purity (from Raman).

Wide temperature range measurements of the resistivity (ρ) for 200 °C ≤ T_S ≤ 600 °C are shown in Figure 4a on a log–linear plot. Although all $\rho(T)$ curves exhibit monotonic semiconducting-like behavior, the evolution with T_S is nontrivial. Specifically, for T_S ≤ 450 °C

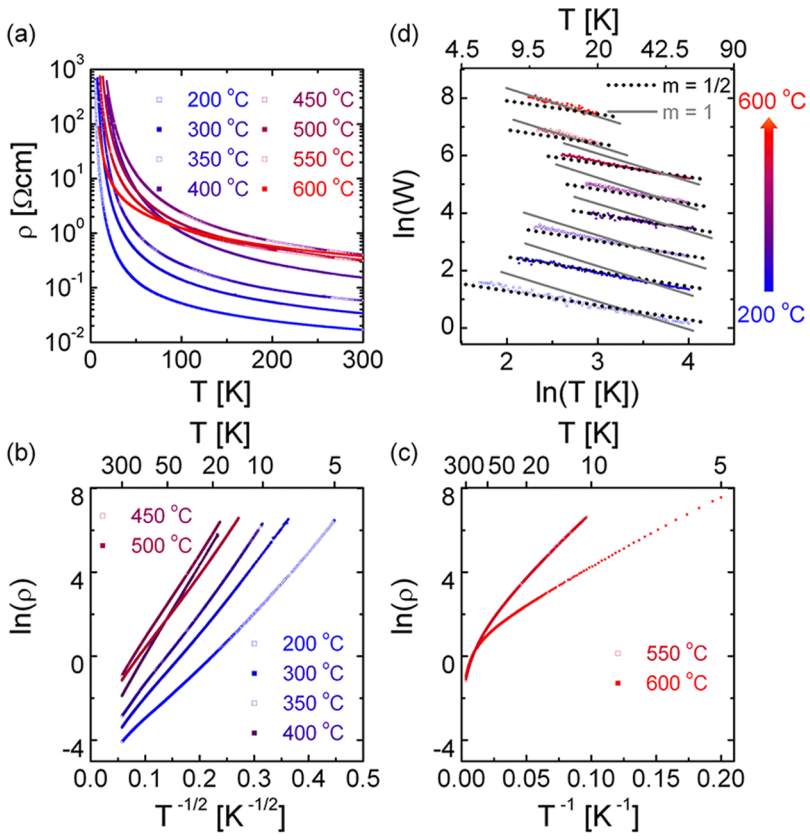

Figure 4. Temperature-dependent resistivity behavior. Temperature dependence of the resistivity (ρ) of 110 nm-thick FeS_2 films sulfidized at temperatures of 200−600 °C. The data are plotted as (a) ρ (log scale) *vs* T (all films), (b) ln ρ *vs* $T^{-1/2}$ (for sulfidation temperatures 500 °C and below), and (c) ln ρ *vs* T^{-1} (for sulfidation temperatures 550 °C and above). (d) ln W *vs* ln T is plotted in the low T region, where $W = -\mathrm{d}\ln\rho/\mathrm{d}\ln T$. Slopes of $m = {}^1/_2$ and 1 are shown for comparison, where m is the exponent in $\rho = \rho_0 \exp(T_0/T)^m$. The curves have been vertically displaced for clarity.

both the low and high T values of ρ increase monotonically with T_S, while for $T_S > 450$ °C the 300 K ρ values saturate, but the low T resistivity actually *decreases* with increasing T_S. This is depicted more clearly in Figure 5a. We immediately note the obvious correlation with the structural data (Figure 3), specifically the importance of the 450 °C temperature scale. Figure 4b,c demonstrate that this abrupt change in resistivity behavior at $T_S \approx$ 450 °C is in fact due to a change in the functional form of $\rho(T)$. Lower T_S samples (Figure 4b) exhibit linear behavior at low T on a ln(ρ) vs $T^{-1/2}$ plot, implying a T dependence of the form $\rho = \rho_0 \exp(T_0/T)^{1/2}$, where ρ_0 is the $T \rightarrow \infty$ value of ρ, and T_0 is a characteristic temperature. In contrast, higher T_S samples (Figure 4c), particularly the 600 °C limiting case, approach linearity at low T on a ln(ρ) vs T^{-1} plot, implying a simple activated dependence, $\rho = \rho_0{}^A \exp(E_A/(k_B T))$, where $\rho_0{}^A$ is the $T \rightarrow \infty$ value of ρ, and E_A is the activation energy. This conclusion is reinforced *via* a quantitative, unbiased analysis using the logarithmic derivative method, where $w = -\mathrm{d}(\ln\rho)/\mathrm{d}(\ln T)$ is plotted vs ln T in order to linearize $\rho = \rho_0 \exp(T_0/T)^m$, yielding the exponent, m, from the slope. This is shown, in the low T region, in Figure 4(d), where slopes of $m = 1/2$ and 1 are also shown for comparison. The crossover from $m \approx {}^1/_2$ to $m \approx 1$ with increasing T_S is clear, the separatrix between the two regimes lying around 450 °C. This is shown more explicitly in Figure 5b, where the T_S dependence of the best-fit value of m at low T is plotted. It must be emphasized that we are focusing here on the low T asymptotic behavior. As shown in Figure 4b,c, and discussed in more detail below, deviations from these forms do occur at higher T, and are in fact expected. Figure 5 panels c and d further plot the T_S dependence of the parameters ρ_0, T_0, and ρ_A, E_A, from the low T_S and high T_S regions, respectively. In all cases the crossover at 400−450 °C is quite clear.

The central question at this stage is the *origin* of the low T_S ($m \approx {}^1/_2$) and high T_S ($m \rightarrow 1$) low temperature transport behavior, and indeed the crossover between the two. Straightforwardly, we interpret the simple activated ($m \approx 1$) behavior approached at high T_S in terms of conventional semiconductor transport, likely associated with shallow dopants or band-tail conduction. The E_A values (~5 meV) are consistent with this interpretation, as is the order of magnitude of $\rho_0{}^A$ (ref 27). Given the small values of E_A the curvature seen in Figure 4c at higher T is unsurprising and indicates a gradual crossover to higher activation energy transport at higher T, as would be expected. The $m = {}^1/_2$

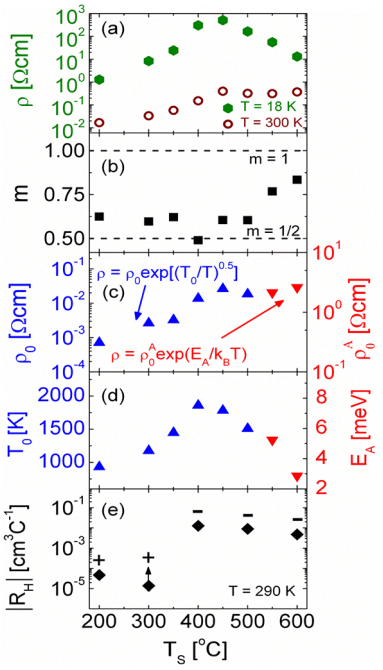

Figure 5. Transport summary. Sulfidation temperature (T_S) dependence of (a) the 18 and 300 K values of the resistivity, (b) the exponent, m, in $\rho = \rho_0 \exp(T_0/T)^m$, (c) the resistivity prefactors extracted from fits to $\rho = \rho_0 \exp(T_0/T)^{1/2}$ (left axis) and $\rho = \rho_0^A \exp(E_A/(k_BT))$ (right axis), (d) the characteristic temperature (T_0) and activation energy (E_A) extracted from fits to these forms, and (e) the magnitude of the 290 K Hall coefficient, R_H. In panel b, the horizontal dashed lines indicate the special values of $m = {}^1/_2$ and 1. In panel e, the ± symbols indicate the sign of the Hall coefficient. Note that, as indicated by the arrow, the T_S = 300 °C data point represents simply an estimate for an upper bound for the very low R_H value obtained.

behavior at low T_S is more challenging. This behavior *could* be interpreted in terms of Efros-Shklovskii variable-range hopping (ES VRH).[27] In ES VRH, the Coulomb interaction effects result in a soft-gapped density of states around the Fermi energy leading to $\rho = \rho_0 \exp(T_0/T)^{1/2}$, with $T_0 = 2.8e^2/(\kappa k_B L_C)$, where κ is the dielectric constant and L_C is the carrier localization length.[27] However, an identical T dependence also arises for thermally assisted tunneling between nanoscopic conductive regions embedded in a more insulating matrix (often referred to as inter-granular hopping (IGH)), due to the Coulomb energy penalty associated with single carrier charging.[28,29] This mechanism must be explicitly considered here as such a nanoscale inhomogeneity in conductivity is certainly plausible, particularly in polycrystalline films synthesized *via* a diffusion-limited reaction with sulfur. IGH has even been employed as a method to *detect* such inhomogeneity.[30] We argue below that a strong case can in fact be built in favor of the IGH scenario over ES VRH. Note that in either case (VRH or IGH), a gradual crossover to other forms of (nonhopping) conduction is expected in the higher T limit.

The first point in favor of IGH is that the observed T_0 values are difficult to reconcile with ES hopping. In ES VRH the maximum T_0 occurs in the insulating limit, where κ has no electronic enhancement and L_C takes its limiting value, the Bohr radius.[27] Using literature values for κ (ref 31) and the effective mass,[32] and a hydrogenic model for the Bohr radius, we obtain $T_{0max} \approx 1800$ K for n-type[33] FeS_2. At higher doping κ and L_C diverge as the insulator−metal transition is approached, rapidly decreasing T_0 (ref 27). In disordered polycrystalline films that are anticipated to be heavily doped (as confirmed below) we thus expect $T_0 \ll 1800$ K. As can be seen from Figure 5d this is not the case; T_0 lies in the 1000−2000 K range. A second strong argument against ES VRH is provided by magnetoresistance (MR) measurements, as detailed in the Supporting Information. In perpendicular fields diamagnetic wave function shrinkage leads to rapid decreases in wave function overlap with increasing magnetic field (H) (ref 27), and thus to large positive MR. This MR follows $\ln[\rho(H)/\rho(0)] = t(e/ch)^2H^2L_C^4(T/T_0)^{-1.5}$ for ES VRH in the weak field limit, with $t = 0.0015$ (ref 27). We thus expect, as has been verified in numerous systems,[27] a large positive MR, growing monotonically with decreasing T and increasing H. As shown in the Supporting Information, this is not the case in our films. While the MR *is* positive at $T_S = 400$ °C, its T dependence is qualitatively inconsistent with expectations, saturating at ~1.5% at 15 K. This discrepancy between experiment and ES VRH theory is even more acute for films synthesized at T_S = 200 °C, where the MR is nonmonotonic with T, has a complex H dependence, and even changes sign below 10 K. In short, both the energy scale associated with $\rho(T)$, and the behavior of $\rho(T,H)$, are inconsistent with ES VRH.

On the basis of the above, interpretation of $\rho = \rho_0 \exp(T_0/T)^{1/2}$ behavior in terms of IGH is clearly favored, directly implicating nanoscale spatial variations in conductivity. Given our diffusion-limited synthesis conditions one obvious scenario is the retention of nanoscopic conductive S-deficient cores (of Fe, $FeS_{1\pm x}$, or Fe_3S_4 (ref 34), with volume fractions beneath WAXRD detection limits, at the center of nominally stoichiometric FeS_2 grains. Magnetometry provides a sensitive probe of such a possibility as the Fe^{2+} in FeS_2 exists in a nonmagnetic ($S = 0$, $t_{2g}^6e_g^0$) configuration [see ref 26 for example], whereas Fe, $FeS_{1\pm x}$ and Fe_3S_4 exhibit magnetic order. Magnetization (M) *vs* H loops were thus collected on T_S = 200 and 400 °C samples (insets to Figure 6a,b). Remarkably, the 200 °C film exhibits clear ferromagnetic response, with finite remnance and coercivity, and a small but significant saturation magnetization of 0.04 μ_B/Fe. The main panel of Figure 6a displays $M(T)$ measured at H = 100 Oe (after both field cooling (FC) and zero field cooling (ZFC)), demonstrating superparamagnetic behavior. The ferromagnetism is thus not uniformly distributed but is confined to small volumes. These volumes apparently become thermally unstable (on the time scale of the measurement) at a blocking temperature, T_B, around 78 K.

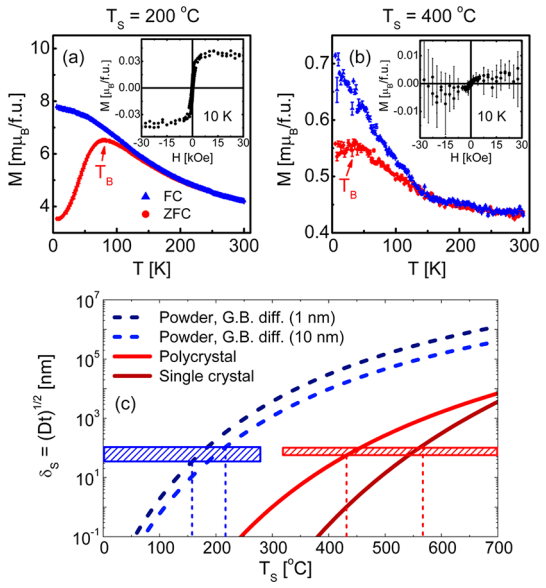

Figure 6. Magnetometry and sulfur diffusion. Panels a and b show the measuring temperature (T) dependence of the magnetization of 110 nm-thick FeS_2 films sulfidized at 200 and 400 °C. The data were acquired in H = 100 Oe after zero field cooling (ZFC) and field cooling (FC) in 100 Oe. The insets show 10 K hysteresis loops. Panel c displays the temperature dependence of the diffusion length ($\delta_S = (D(T_S)t)^{1/2}$, where $D(T_S)$ is the diffusion coefficient and t is time (fixed at 8 h)), for S diffusion in Fe. The data are shown both for grain boundary diffusion (assuming grain boundary widths of 1 and 10 nm),[35] and for large grain polycrystal[36] and single crystal Fe[37] (to exemplify bulk diffusion). The shaded region on the left (right) marks the range of relevant thicknesses (grain sizes).

Assuming for the moment that this magnetic signal arises due to metallic Fe, the magnetization we observe can be accounted for by as little as 0.5 vol % of unreacted Fe, a value that lies below our own WAXRD detection limits (see Supporting Information for more details), and likely many such lab XRD systems. Combining this estimated volume fraction with the measured d_{grain}, and assuming the unreacted Fe lies at the core of each grain, a trivial calculation yields a core size, d_{core}, of 10 nm. This is in good agreement with the typical particle sizes for which IGH is detected, and is broadly consistent with the observed T_0 (ref 35). For example, using d_{core} = 10 nm and literature values for κ results in Coulomb charging energies around 10 meV, consistent with the observation of IGH up to 100 s of K. Under the simple assumption of spherical grain cores this d_{core} can also be combined with the known magnetocrystalline anisotropy constant of metallic Fe to predict, with no adjustable parameters, T_B = 72 K. The excellent agreement with the measured value (78 K) confirms that all aspects of these measurements are quantitatively consistent with an Fe metal grain core. Alternatively, repeating these calculations assuming for example that $FeS_{1\pm x}$ is retained in the grain cores yields an impurity phase volume fraction of 20%, and $T_B \approx T_C$ (580 K) (ref 36), both of which are inconsistent with experiment. The situation is similar for Fe_3S_4 (ref 37). We thus definitively rule out $FeS_{1\pm x}$ or Fe_3S_4 grain cores in favor of metallic Fe, although it is possible, perhaps likely,[20] that a thin shell of $FeS_{1\pm x}$ exists between the Fe core and the FeS_2 matrix. Reassuringly, at a higher T_S of 400 °C, where diffusion is expected to have improved, both the saturation magnetization and $M(T)$ FC/ZFC splitting are dramatically reduced (Figure 6b), to the point where they are barely detectable. At T_S = 600 °C we detect no magnetization above background. The crossover from IGH to conventional activated transport, our central observation so far, is thus simply interpreted in terms of an evolution from nanoscopic unreacted Fe cores in an FeS_2 matrix to nominally single-phase uniform FeS_2. It should be emphasized that such IGH transport ideas could well be applicable beyond *ex situ* sulfidation methods, and that any situation that could lead to significant nanoscale variations in Fe/S ratio could potentially result in IGH transport. It is worth noting in fact that in our recent prior work on reactively sputtered FeS_2 a $\rho = \rho_0 \exp (T_0/T)^{1/2}$ dependence was also observed.[26] Further work will be required to fully understand the generality of such behavior in FeS_2 synthesized by other methods.

The scenario discussed above is in fact supported by a simple analysis of S diffusion in Fe. As in the case of sulfidation of Co[38] we believe that the reaction to form the disulfide is diffusion-limited, proceeding in two steps; grain boundary diffusion to enable widespread ingress of S, followed by bulk diffusion through the grain interior.[20,38] Literature data on these two processes are shown in Figure 6c, which plots the T dependence of the diffusion length, $\delta_S = (D(T_S)t)^{1/2}$, where D is the diffusion constant for S in Fe, and t is time (fixed at 8 h in this case). Data are shown both for grain boundary diffusion (assuming grain boundary widths of 1 and 10 nm (ref 39)), and for large grain polycrystal[40] and single crystal[41] Fe (to exemplify bulk diffusion). Marking the film thickness and grain size ranges relevant to our case (*i.e.*, 33 to 110 nm, and 55 to 110 nm, respectively)[42] with horizontal bands, the temperature ranges of intersection with the $\delta_S(T)$ curves for the grain boundary and bulk diffusion cases yield simple estimates for the T_S at which sulfidation is expected to commence, and near completion. This process, which is shown in Figure 6c, yields 160−220 °C and 430−560 °C, respectively. The agreement with experiment (200 and 450 °C) is remarkable, despite the fact that we have ignored some potential complicating factors, particularly S diffusion rates in intermediary $FeS_{1\pm x}$, and in FeS_2 itself.[20]

Our conclusion of a T_S-dependent crossover from intergranular hopping to conventional transport due to diffusion-driven improvements in nanoscale homogeneity provides important context for the final interesting result of this study. This is shown in Figure 5e, where the magnitude of the 290 K Hall coefficient (R_H), as extracted from Hall measurements described in the

Supporting Information, is shown as a function of T_S. The data reveal two surprising observations: a 3 order of magnitude increase in $|R_H|$ at $T_S \approx 400$ °C, and a coincident abrupt sign reversal from positive at low T_S to negative at high T_S. (The ± signs adjacent to each point indicate the sign of R_H). Naïve interpretation within the simplest model (*i.e.*, a single dominant carrier type, in diffusive transport) would suggest a crossover from p-type to n-type. However, in the hopping transport regime it is well-known that the Hall effect is strongly suppressed, that it evolves with *T*, H, and carrier density in a complex manner (preventing simple extraction of the carrier density),[43,44] and that it can even result in a sign for the Hall coefficient that no longer reflects the true sign of the charge carriers.[43,44] We thus believe that the small $|R_H|$ observed at $T_S < 400$ °C is due to the occurrence of hopping transport, and that the positive sign must *not* be interpreted in terms of p-type conduction. The rapid increase in $|R_H|$ around $T_S = 400$ °C signals the crossover from the hopping to diffusive transport regime, where the Hall effect can be more simply interpreted. The conduction in this regime is found to be definitively n-type. Converting these R_H values at $T_S \geq 400$ °C to electron densities yields 5×10^{20} to 1×10^{21} cm^{-3}. (Note here that we have used the simplest model where a single carrier type is assumed dominant; our observation of a linear Hall effect to 9 T at all temperatures (see Supporting Information) is important in this regard). These very heavy doping levels result in correspondingly low electron mobilities (0.1 to 0.01 cm^2 V^{-1} s^{-1} for the three films shown in Figure 5e), the largest mobility we have obtained in as-prepared *ex situ* sulfidized FeS_2 films lying around 1 cm^2 V^{-1} s^{-1}. Note that both the absolute value of the mobility (0.1−1 cm^2 V^{-1} s^{-1}), and its temperature dependence (see Supporting Information), indicate proximity to the crossover region between hopping and diffusive transport regimes. This is consistent with close examination of Figure 5b which suggests that perfect adherence to $\rho = \rho_0^A \exp(E_A/(k_B T))$ is not yet achieved even at $T_S = 600$ °C.

CONCLUSIONS

We conclude with some comments on the implications of these findings for future research on FeS_2 for PV applications. First, and particularly for synthesis routes that may result in diffusion limited conditions, it is clear from this work that attainment of conventional diffusive semiconductor transport in FeS_2 films is nontrivial, requiring significant attention to nanoscale chemical homogeneity. Second, it is also clear that considerable caution must be exercised in the interpretation of Hall measurements, particularly with respect to the determination of the sign of the charge carriers. In this context we note (i) that some reports of p-type conduction in FeS_2 films have been made in the absence of temperature-dependent measurements definitively establishing diffusive transport, and (ii) that an intriguing correlation exists, both in bulk and thin film FeS_2, between low mobility and apparent p-type transport. With regard to the latter, recent work on single crystals has even revealed a temperature-dependent sign reversal of the Hall effect.[45] Future work, combining a variety of synthesis methods with detailed electronic characterization, should be able to resolve many of these issues, hopefully providing the long-elusive understanding of the doping and transport mechanisms in FeS_2 films. On this note we would like to point out that while the mobilities reported in this paper for *ex situ* sulfidized films remain modest (~1 cm^2 V^{-1} s^{-1} or less), considerable room for improvement remains, particularly by improving synthesis and postdeposition treatment protocols. Indeed, future work refining synthesis and processing techniques for appropriate defect management will be required to reduce the carrier densities to workable levels for PV devices, and to improve mobility. The origin of the n-type behavior seen in this work is also an open issue that will require further work. While there are many possible origins, uncontrolled dopants in the Fe starting material, and out-diffusion of dopants from the substrate are obvious possibilities that should be further investigated.

METHODS

FeS_2 thin films were fabricated *via ex situ* sulfidation, as detailed in the Supporting Information. Briefly, sputtered Al_2O_3-(0001)/Fe(110) films (33 nm thick, deposited at 300 °C) were placed in quartz tubes (8 cm^3 volume) with 1.0 ± 0.1 mg of 99.999% pure S, evacuated to 1×10^{-6} Torr, sealed, and heated for 8 h at a sulfidation temperature, T_S, between 100 and 800 °C. Simple calculations (see SI for more details) give a resulting S vapor pressure of 2 Torr at 200 °C, 25 Torr at 400 °C, and 45 Torr at 700 °C. After synthesis, the films were thoroughly characterized structurally and chemically (see Supporting Information for details) *via* wide-angle X-ray diffraction (WAXRD), scanning electron microscopy/energy dispersive spectroscopy (SEM/EDS), depth-profiled auger electron spectroscopy (AES), and Raman spectroscopy. Electronic transport (see Supporting Information for details) employed In contacts in a 4-wire van der Pauw configuration using ac (13.7 Hz) and dc excitation. Measurements were made from 5−300 K, in magnetic fields up to 9 T, with extensive checks for Ohmicity, contact resistance, and self-heating. More details are provided in the Supporting Information. Magnetometry was done in a SQUID magnetometer from 5−300 K in fields to 7 T.

Conflict of Interest: The authors declare no competing financial interest.

Acknowledgment. Work supported by the UMN Initiative for Renewable Energy and the Environment, and in part by the MRSEC program of the NSF under DMR-0819885. M.J. was supported by NSF through CBET-0931145. Parts of this work were carried out in the UMN Characterization Facility, which receives partial support from NSF through the MRSEC program.

Supporting Information Available: Additional film synthesis details, additional structural characterization data from X-ray diffraction, Auger electron spectroscopy and Raman spectroscopy, additional transport and magnetotransport data, additional Hall effect data, and additional information on magnetometry measurements and associated analysis. This material is available free of charge *via* the Internet at http://pubs.acs.org.

REFERENCES AND NOTES

1. Wadia, C.; Alivisatos, A. P.; Kammen, D. M. Materials Availability Expands the Opportunity for Large-Scale Photovoltaics Deployment. *Environ. Sci. Technol.* **2009**, *43*, 2072–2077.
2. Ennaoui, A.; Fiechter, S.; Pettenkofer, Ch.; Alonso-Vante, N.; Büker, K.; Bronold, M.; Höpfner, Ch.; Tributsch, H. Iron Disulfide for Solar Energy Conversion. *Sol. Energy Mater. Sol. Cells* **1993**, *29*, 289–370.
3. Yu, L.; Lany, S.; Kykyneshi, R.; Jieratum, V.; Ravichandran, R.; Pelatt, B.; Altschul, E.; Platt, H. A. S.; Wager, J. F.; Keszler, D. A.; *et al.* Iron Chalcogenide Photovoltaic Absorbers. *Adv. Energy Mater.* **2011**, *1*, 748–753.
4. Berry, N.; Cheng, M.; Perkins, C. L.; Limpinsel, M.; Hemminger, J. C.; Law, M. Atmospheric-Pressure Chemical Vapor Deposition of Iron Pyrite Thin Films. *Adv. Energy Mater.* **2012**, *2*, 1124–1135.
5. Schieck, R.; Hartmann, A.; Fiechter, S.; Könenkamp, R.; Wetzel, H. Electrical Properties of Natural and Synthetic Pyrite (FeS_2) Crystals. *J. Mater. Res.* **1990**, *5*, 1567–1572.
6. Birkholz, M.; Fiechter, S.; Hartmann, A.; Tributsch, H. Sulfur Deficiency in Iron Pyrite (FeS_{2-x}) and its Consequences for Band-Structure Models. *Phys. Rev. B* **1991**, *43*, 11926–11936.
7. Sun, R.; Chan, M. K. Y.; Ceder, G. First-Principles Electronic Structure and Relative Stability of Pyrite and Marcasite: Implications for Photovoltaic Performance. *Phys. Rev. B* **2011**, *83*, 235311.
8. Hu, J.; Zhang, Y.; Law, M.; Wu, R. First-Principles Studies of the Electronic Properties of Native and Substitutional Anionic Defects in Bulk Iron Pyrite. *Phys. Rev. B* **2012**, *85*, 085203.
9. Bi, Y.; Yuan, Y.; Exstrom, C. L.; Darveau, S. A.; Huang, J. Air Stable, Photosensitive, Phase Pure Iron Pyrite Nanocrystal Thin Films for Photovoltaic Application. *Nano Lett.* **2011**, *11*, 4953–4957.
10. Puthussery, J.; Seefeld, S.; Berry, N.; Gibbs, M.; Law, M. Colloidal Iron Pyrite (FeS_2) Nanocrystal Inks for Thin-Film Photovoltaics. *J. Am. Chem. Soc.* **2011**, *133*, 716–719.
11. Cabán-Acevedo, M.; Faber, M. S.; Tan, Y.; Hamers, R. J.; Jin, S. Synthesis and Properties of Semiconducting Iron Pyrite (FeS_2) Nanowires. *Nano Lett.* **2012**, *12*, 1977–1982.
12. Morrish, R.; Silverstein, R.; Wolden, C. A. Synthesis of Stoichiometric FeS_2 through Plasma-Assisted Sulfurization of Fe_2O_3 Nanorods. *J. Am. Chem. Soc.* **2012**, *134*, 17854–17857.
13. Zhang, Y. N.; Hu, J.; Law, M.; Wu, R. Q. Effect of Surface Stoichiometry on the Band Gap of the Pyrite FeS_2 (100) Surface. *Phys. Rev. B* **2012**, *85*, 085314.
14. Bausch, S.; Sailer, B.; Keppner, H.; Willeke, G.; Bucher, E.; Frommeyer, G. Preparation of Pyrite Films by Plasma-Assisted Sulfurization of Thin Iron Films. *Appl. Phys. Lett.* **1990**, *57*, 25–27.
15. Ferrer, I. J.; Sánchez, C. Characterization of FeS_2 Thin Films Prepared by Thermal Sulfidation of Flash Evaporated Iron. *J. Appl. Phys.* **1991**, *70*, 2641–2647.
16. Heras, C. de las; Vidales, J. L. M. de; Ferrer, I. J.; Sánchez, C. Structural and Microstructural Features of Pyrite FeS_{2-x} Thin Films Obtained by Thermal Sulfuration of Iron. *J. Mater. Res.* **1996**, *11*, 211–220.
17. Meng, L.; Liu, Y. H.; Tian, L. Structural, Optical and Electrical Properties of Polycrystalline Pyrite (FeS_2) Films Obtained by Thermal Sulfuration of Iron Films. *J. Cryst. Growth* **2003**, *253*, 530–538.
18. Wan, D.; Wang, Y.; Wang, B.; Ma, C.; Sun, H.; Wei, L. Effects of the Crystal Structure on Electrical and Optical Properties of Pyrite FeS_2 Films Prepared by Thermally Sulfurizing Iron Films. *J. Cryst. Growth* **2003**, *253*, 230–238.
19. Ares, J. R.; Pascual, A.; Ferrer, I. J.; Sánchez, C. Grain and Crystallite Size in Polycrystalline Pyrite Thin Films. *Thin Solid Films* **2005**, *480–481*, 477–481.
20. Pimenta, G.; Kautek, W. Thermodynamic Aspects of Pyrite Film Formation by Sulphur Conversion of Iron. *Thin Solid Films* **1992**, *219*, 37–45.
21. Controversy exists over the extent to which nonstoichiometry is possible in FeS_2 (see for example ref 3.). We use the term "single phase" to mean single phase within the resolution of the various techniques applied here.
22. The surface roughness is found to be below 5 nm over a 2 μm $\times$ 2 μm area, from contact mode AFM.
23. FeS_2 films appear to be susceptible to delamination and cracking, as discussed in refs 24–26.
24. Birkholz, M.; Lichtenberger, D.; Höpfner, C.; Fiechter, S. Sputtering of Thin Pyrite Films. *Sol. Energy Mater. Sol. Cells* **1992**, *27*, 243–251.
25. Meng, L.; Liu, Y. H.; Tian, L. Evolutions of Structure, Composition and Optical Absorption Behavior of Pyrite Films Formed by Sulfurating Iron. *Mater. Res. Bull.* **2003**, *38*, 941–948.
26. Baruth, A.; Manno, M.; Narasimhan, D.; Shankar, A.; Zhang, X.; Johnson, M.; Aydil, E. S.; Leighton, C. Reactive Sputter Deposition of Pyrite Structure Transition Metal Disulfide Thin Films: Microstructure, Transport, and Magnetism. *J. Appl. Phys.* **2012**, *112*, 054328.
27. Shklovskii, B. I.; Efros, A. L. *Electronic Properties of Doped Semiconductors*; Springer Series in Solid-State Sciences; Springer-Verlag: Berlin; New York, 1984.
28. Sheng, P.; Abeles, B.; Arie, Y. Hopping Conductivity in Granular Metals. *Phys. Rev. Lett.* **1973**, *31*, 44–47.
29. Zhang, J.; Shklovskii, B. I. Density of States and Conductivity of a Granular Metal or an Array of Quantum Dots. *Phys. Rev. B* **2004**, *70*, 115317.
30. Kennedy, R. J.; Stampe, P. A.; Hu, E.; Xiong, P.; Molnár, S. von; Xin, Y. Hopping Transport in TiO_2:Co: A Signature of Multiphase Behavior. *Appl. Phys. Lett.* **2004**, *84*, 2832–2834.
31. Husk, D. E.; Seehra, M. S. Dielectric Constant of Iron Pyrite (FeS_2). *Solid State Commun.* **1978**, *27*, 1147–1148.
32. Altermatt, P. P.; Kiesewetter, T.; Ellmer, K.; Tributsch, H. Specifying Targets of Future Research in Photovoltaic Devices Containing Pyrite (FeS_2) by Numerical Modelling. *Sol. Energy Mater. Sol. Cells* **2002**, *71*, 181–195.
33. We use the n-type case as an example at this point. n-Type behavior is confirmed later in the paper.
34. Most, possibly all, such phases are indeed conductive (*e.g.*, FeS, $Fe_{1+\delta}S$, Fe_7S_8, Fe_3S_4, *etc.*)
35. Abeles, B.; Sheng, P.; Coutts, M. D.; Arie, Y. Structural and Electrical Properties of Granular Metal Films. *Adv. Phys.* **1975**, *24*, 407–461.
36. We assumed here the phase in the vicinity of Fe_1S_1 with the largest magnetization [pyrrhotite – see Dekkers, M. J. Magnetic Properties of Natural Pyrrhotite Part I: Behaviour of Initial Susceptibility and Saturation-Magnetization-Related Rock-Magnetic Parameters in a Grain-Size Dependent Framework. *Phys. Earth Planet. Inter.* **1988**, *52*, 376–393]. Assuming the existence of other phases with lower magnetization would yield even larger volume fractions, again clearly inconsistent with our structural characterization.
37. Assuming Fe_3S_4 is present and using the known magnetization and anisotropy constant [see Roberts, A. P.; Chang, L.; Rowan, C. J.; Horng, C.-S.; Florindo, F. Magnetic Properties of Sedimentary Greigite (Fe_3S_4): An Update. *Rev. Geophys.* **2011**, *49*, 1002–1046], we obtain T_B = 200–300 K, again inconsistent with our data.
38. Manno, M.; Frakie, R.; Leighton, C. Synthesis and Characterization of Highly Spin-Polarized Single-Phase $Co_{1-x}Fe_xS_2$ Films. *J. Appl. Phys.* **2009**, *105*, 093912–9.
39. Gruzin, P. L.; Mural, V. V.; Fokin, A. P. Diffusion of Sulfur in Alpha-Iron. *Fiz. Met. Metalloved.* **1972**, *34*, 1326–1328.
40. Ainslie, N. G.; Seybolt, A. U. Diffusion and Solubility of Sulphur in Iron and Silicon–Iron Alloys. *J. Iron Steel Inst.* **1960**, *194*, 341–350.
41. Arabczyk, W.; Militzer, M.; Müssig, H.-J.; Wieting, J. Activation Energy of Sulphur Diffusion in Ferromagnetic α-Iron

Determined by Surface Segregation Studies. *Scr. Metall.* **1986**, *20*, 1549–1554.
42. For such a simple estimate, the length scale relevant for the grain boundary diffusion is the film thickness, which is 33 nm initially, rising to 110 nm after sulfidation. The length scale relevant for the bulk diffusion is the grain size, which is in the range 55 to 110 nm.
43. Le Comber, P. G.; Jones, D. I.; Spear, W. E. Hall Effect and Impurity Conduction in Substitutionally Doped Amorphous Silicon. *Philos. Mag.* **1977**, *35*, 1173–1187.
44. Galperin, Y. M.; German, E. P.; Karpov, V. G. Hall Effect under Hopping Conduction Conditions. *Sov. Phys. JETP* **1991**, *72*, 193–200.
45. Berry, N.; Limpinsel, M.; Law, M., private communication, **2012**.